Three-dimensional linear instability in pressure-driven two-layer channel flow of a Newtonian and a Herschel–Bulkley fluid

K. C. Sahu[1,a)] and O. K. Matar[2]

[1]*Department of Chemical Engineering, Indian Institute of Technology Hyderabad, Andhra Pradesh 502205, India*
[2]*Department of Chemical Engineering, Imperial College London, London SW7 2AZ, United Kingdom*

The three-dimensional linear stability characteristics of pressure-driven two-layer channel flow are considered, wherein a Newtonian fluid layer overlies a layer of a Herschel–Bulkley fluid. We focus on the parameter ranges for which Squire's theorem for the two-layer Newtonian problem does not exist. The modified Orr–Sommerfeld and Squire equations in each layer are derived and solved using an efficient spectral collocation method. Our results demonstrate the presence of three-dimensional instabilities for situations where the square root of the viscosity ratio is larger than the thickness ratio of the two layers; these "interfacial" mode instabilities are also present when density stratification is destabilizing. These results may be of particular interest to researchers studying the transient growth and nonlinear stability of two-fluid non-Newtonian flows. We also show that the "shear" modes, which are present at sufficiently large Reynolds numbers, are most unstable to two-dimensional disturbances. © *2010 American Institute of Physics*.
[doi:10.1063/1.3502023]

I. INTRODUCTION

Two-fluid flows are common in many practical applications, such as the cleaning of first-moving consumer good plants, transportation of crude oil in pipelines,[1] mixing of liquids using centerline injectors, up-stream of static mixers,[2] and the removal of highly viscous or elastoviscoplastic material adhering to pipes by using fast-flowing water streams.[3] The two-dimensional instability of two-fluid Poiseuille flows has been addressed by many authors via asymptotic[4–7] and linear stability analyses,[8–11] as well as experimental techniques.[12] An extended review can be found in Ref. 13.

Recently, Sahu *et al.*[14] studied the linear instability of two-dimensional disturbances in a pressure-driven two-layer channel flow, wherein a Newtonian fluid layer overlies a layer of a Herschel–Bulkley fluid. Their results indicate that increasing the yield stress, prior to the formation of unyielded zones, and shear-thickening tendency are destabilizing. They also conducted an energy analysis to study the mechanism of this instability. Frigaard *et al.*[11] studied the two-dimensional linear stability of two-layer Poiseuille flow of two Bingham fluids in which only a fraction of the Bingham fluid has yielded. Unlike in the study of Sahu *et al.*,[14] the case studied by Frigaard *et al.*[11] involves an unyielded region between the Newtonian fluid and the yielded part of the Bingham fluid. Interfacial waves would not develop under such conditions; this suppression of interfacial modes then leads to superstable two-layer flows,[11,15] similar to single-fluid pressure-driven flows.[16,17] The effect of three-dimensional disturbances on the stability of pressure-driven channel flow, however, has received less attention than that of two-dimensional ones.

Squire[18] studied the stability of viscous fluid flow through parallel walls and found that every unstable three-dimensional disturbance is associated with a more unstable two-dimensional disturbance at a lower value of the Reynolds number. This result is commonly known as "Squire's theorem"[19] and the connection between the two- and three-dimensional disturbances is known as "Squire's transformation." Extending this to two superposed fluids in plane Poiseuille flow, Yiantsios and Higgins[5] showed that three-dimensional disturbances are associated with smaller Reynolds numbers, and larger capillary contributions and density stratifications. The larger capillary contributions are stabilizing for all parameter values, as is density stratification provided the density of the upper fluid is lower than that of the lower one. Thus, although a Squire's transformation can exist for all flow parameters, a Squire's theorem can only exist provided the Reynolds number has a destabilizing effect. In the absence of surface tension and gravitational effects, Squire's theorem is valid for $t_r > \sqrt{m}$ since the Reynolds number is destabilizing; here, t_r is the thickness ratio of the two fluids and m is the viscosity ratio. For $t_r < \sqrt{m}$, the Reynolds number is stabilizing and Squire's theorem no longer exists. This is also true in the presence of destabilizing density stratification. As remarked by Yiantsios and Higgins[5] in the absence of a Squire's theorem, it is necessary to perform a three-dimensional linear stability analysis in order to determine whether or not two-dimensional disturbances correspond to the most dangerous ones.

Malik and Hooper[20] recently studied the effect of three-dimensional disturbances on two-fluid channel flow, wherein both the fluids are Newtonian. Using an energy analysis they showed that maximum amplification of the disturbances is due to the "lift-up effect" as in case of single phase flow. They also found that, for some parametric regime, the
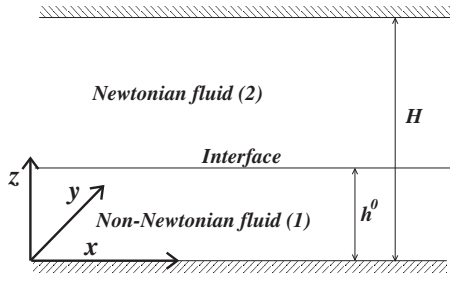
a)Electronic mail: ksahu@iith.ac.in.

FIG. 1. Schematic of a two-layer flow in a channel of height H, where h represents the thickness of the lower, non-Newtonian fluid.

maximum disturbance energy growth is associated with three-dimensional disturbances. In a series of papers, Nouar and co-workers[15,21,22] studied the three-dimensional linear instability of pressure-driven channel flow of a Bingham fluid. Frigaard and Nouar[21] investigated the effects of increasing Bingham number Bn on the stability of plane Poiseuille flow using energy bounds. They achieved three-dimensional instability as $Bn \to \infty$ for a Reynolds number bound of the form $Re = O(Bn^{3/4})$. Nouar et al.[15] studied this problem using both modal and nonmodal approaches; they found the flow to be always linearly stable. To identify a possible pathway toward transition Nouar et al.,[22] revisited this problem and found transient amplification to be the main mechanism of transition in this case.

In the present study, we extend the previous work of Malik and Hooper,[20] and Frigaard and Nouar[21] to examine the three-dimensional linear stability of two-layer plane Poiseuille flow wherein a Newtonian layer flows past a layer of a Herschel–Bulkley fluid. We focus on the range of parameters for which Squire's theorem does not exist in the Newtonian two-layer case; here, by "Newtonian" we refer to the flow in the absence of a yield stress and a constant, shear-rate-independent viscosity in both layers. Through a linear stability analysis, we demonstrate the presence of three-dimensional instabilities corresponding to "interfacial modes" that are more unstable than their two-dimensional counterparts; this was not possible for the "shear modes." Our results may be of particular interest to researchers studying the transient growth of disturbances and their nonlinear growth in two-fluid flows.

The rest of this paper is organized as follows. Details of the problem formulation are provided in Sec. II, and the results of the linear stability analysis are presented in Sec. III. Concluding remarks are provided in Sec. IV.

II. FORMULATION

We consider a pressure-driven immiscible two-fluid channel flow, wherein the upper and lower fluids are assumed to be Newtonian and non-Newtonian, respectively; both fluids are incompressible. The Herschel–Bulkley model is employed to describe the rheological characteristics of the non-Newtonian fluid. A rectangular coordinate system (x, y, z) is used to model this flow, where x, y, and z denote the streamwise, spanwise, and wall-normal coordinates, respectively, as shown in Fig. 1. The rigid and impermeable channel walls are located at $z=0$ and $z=H$, respectively; the

sharp interface, which separates the immiscible fluids, is at $z=h^0$. The height of the channel, H, and $V \equiv Q/H$ are used as the length and velocity scales, respectively, in order to non-dimensionalize the equations of motion, where Q denotes the total flow rate. The viscosity and density have been scaled with those of the upper, Newtonian fluid, i.e., μ_2 and ρ_2, respectively. The reduced dimensionless pressure P_i in fluid i is related to the corresponding total dimensional pressure p_i through

$$P_i = \frac{H}{\mu_2 V}[p_i + \rho_i g(z-h)] \quad (i=1,2), \tag{1}$$

where g is the gravitational acceleration. The subscripts "1" and "2" are used to represent quantities associated with the lower and upper fluids, respectively.

The dimensionless viscosity of the non-Newtonian fluid is given by

$$\mu_1 = m\Pi^{n-1} + Bn\Pi^{-1}, \tag{2}$$

where $\Pi \equiv (2E_{ij}E_{ij})^{1/2}$ represents the second invariant of the rate of strain tensor, $E_{ij} = \frac{1}{2}(\partial u_i/\partial x_j + \partial u_j/\partial x_i)$; $Bn \equiv \tau_0 H/\mu_2 V$ is a Bingham number and $m \equiv \mu_2^{-1}\kappa(V/H)^{n-1}$ is a viscosity ratio, wherein τ_0 is the yield stress; κ and n are the consistency and flow index, respectively. Note that we restrict the analysis to sufficiently low value of τ_0 so that there are no unyielded regions in $0 \le y \le h$ (Ref. 14).

A. Base state

The base state whose linear stability characteristics will be analyzed, corresponds to a steady, parallel, fully developed flow in both the layers separated by a flat interface, i.e., $h=h^0$ and $V=W=0$; $U_i(i=1,2)$ is only a function of z and pressure distribution $(P_1=P_2=P)$ is linear in x

$$U_1 = \frac{n}{n+1} \frac{(dP/dx)^{-1}}{m^{1/n}}\left[\frac{dP}{dx}z + c_3 - Bn\right]^{(n+1)/n} + c_4, \tag{3}$$

$$U_2 = \frac{dP}{dx}\frac{z^2}{2} + c_1 z + c_2. \tag{4}$$

We obtained Eqs. (3) and (4) by integrating the steady, fully developed dimensionless Navier–Stokes equations, imposing the no-slip conditions at the walls and demanding continuity of velocity and the tangential component of the stress at the interface. The pressure gradient, dP/dx and the integration constants, c_1, c_2, c_3, and c_4 are obtained by solving the following simultaneous equations:

$$\frac{n(dP/dx)^{-1}}{(n+1)m^{1/n}}\left\{\left[\frac{dP}{dx}h^0 + c_3 - Bn\right]^{(n+1)/n} - [c_3 - Bn]^{(n+1)/n}\right\}$$
$$-\frac{1}{2}\frac{dP}{dx}(h^{02}-1) - c_1(h^0-1) = 0,$$

$$c_3 = c_1, \quad c_2 = -\frac{1}{2}\frac{dP}{dx} - c_1, \tag{5}$$

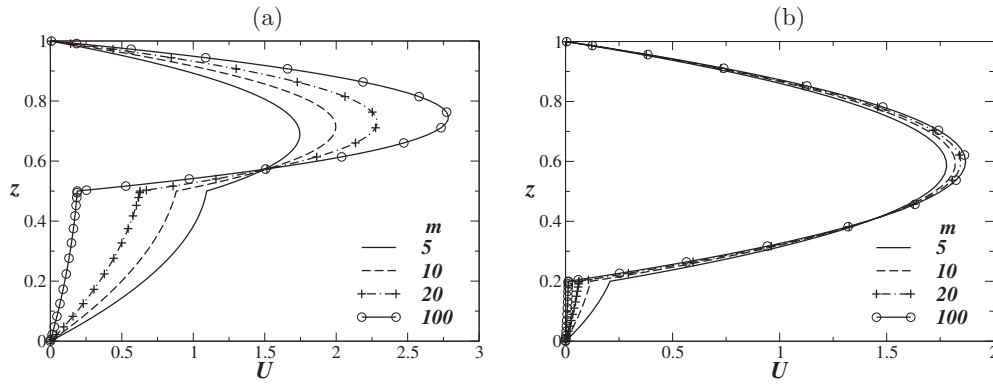$$c_4 = -\frac{n(dP/dx)^{-1}}{(n+1)m^{1/n}}[c_1 - Bn]^{(n+1)/n},$$

FIG. 2. Basic state profiles of the steady, streamwise velocity component for $h^0=0.5$, (a), and $h^0=0.2$ (b), respectively. The rest of the parameter values are Re=100, Bn=5, and $n=1$.

and
$$\int_0^h U_1 dz + \int_h^1 U_2 dz = 1. \tag{6}$$

The pressure gradient, dP/dx, is obtained from the constant volumetric flow rate condition, i.e.,

$$\int_0^{h^0} U_1 dz + \int_{h^0}^1 U_2 dz = 1. \tag{7}$$

It is possible to generate an algebraic relationship between $m, n, h^0, \mathrm{Bn}, dP/dx$ to characterize the case wherein the lower layer is fully yielded by first determining the condition for which the lower layer will just begin to yield: by setting $\Pi=0$. In the base state, $\Pi=dU_1/dz$, which from Eq. (3) is given by

$$\Pi = \frac{dU_1}{dz} = \frac{1}{m^{1/n}} \left(\frac{dP}{dx} z + c_3 - \mathrm{Bn} \right)^{1/n}. \tag{8}$$

$\Pi=0$ for a particular value of z, Y; this is the "yield surface"

$$Y = \frac{\mathrm{Bn} - c_3}{dP/dx}, \tag{9}$$

where dP/dx and $c_3 = c_3(m, n, h^0, \mathrm{Bn}, dP/dx)$ are given by Eqs. (5) and (7), respectively; note that $dP/dx < 0$ in this work. By equating $Y = h^0$, i.e., by assuming that the whole lower layer will yield, we arrive at

$$\mathrm{Bn} - c_3 - h^0 dP/dx = 0, \tag{10}$$

which provides a relationship that can be then be used to determine the appropriate combination of m, n, Bn, h^0, dP/dx for the fully yielded regime.

Typical basic state profiles of the steady, streamwise velocity component for $h^0=0.5$ and $h^0=0.2$ are shown in Figs. 2(a) and 2(b), respectively. The rest of the parameter values are Re=100, Bn=5, and $n=1$. These parameter values are chosen such that they satisfy $h^0/(1-h^0) < \sqrt{m}$ for which there is no Squire's theorem.[5] Inspection of Fig. 2 reveals that increasing the value of m leads to an increase in maximal velocity contrast between the upper and lower fluids.

B. Linear stability analysis

We examine the linear stability of the base state, obtained by solving Eqs. (3) and (4), to infinitesimal, three-dimensional (3D) disturbances. Only the essential steps involved in the derivation of the linear stability equations are included below; a detailed derivation can be found in Appendix A.

Each flow variable is expressed as the sum of a base state and a 3D perturbation,

$$(\tilde{u}_i, \tilde{v}_i, \tilde{w}_i, \tilde{P}_i)(x, y, z, t)$$
$$= [U_i(z), 0, 0, P_i] + (\hat{u}_i, \hat{v}_i, \hat{w}_i, \hat{p}_i)(x, y, z, t), \tag{11}$$

with $i = 1, 2$. Similarly the viscosity, μ_1 and h can be expressed as

$$\mu_1(\pi) = \mu_1^0 + \left. \frac{\partial \mu_1}{\partial \pi} \right|^0 (\pi - \Pi) \equiv \mu_1^0 + \mathcal{S}\hat{\pi}, \tag{12}$$

$$h(x, y, t) = h^0 + \hat{h}, \tag{13}$$

where $\mathcal{S} = (n-1)m\Pi^{n-2} - \mathrm{Bn}\Pi^{-2}$; the linearized form of $\hat{\pi}$ is given by

$$\hat{\pi} = \frac{\partial \hat{u}}{\partial z} + \frac{\partial \hat{w}}{\partial x}, \tag{14}$$

where $\hat{u}$, $\hat{v}$, and $\hat{w}$ denote the streamwise, spanwise, and wall-normal components of the disturbance velocity vector, respectively. The superscript "0" designates the base state quantities. Substitution of Eqs. (11)–(13) into the governing equations followed by subtraction of the base state equations, subsequent linearization, and elimination of the pressure perturbation yields in linear stability equations in terms of primary variables. These equations are reexpressed in terms of the wall-normal perturbation velocity, $\hat{w}_i$, and wall-normal component of vorticity, $\hat{\eta}_i \equiv \partial \hat{u}_i / \partial y - \partial \hat{v}_i / \partial x$, and then decomposed into an amplitude and a wave part by using a normal modes analysis

$$(\hat{w}_i, \hat{\eta}_i, \hat{p}_i, \hat{\pi})(x, y, z, t) = (w_i, \eta_i, p_i, \tilde{\pi})(z)e^{i(\alpha x + \beta y - \Omega t)},$$

(15)

$$\hat{h}(x, y, t) = \tilde{h}e^{i(\alpha x + \beta y - \Omega t)}, \quad i = 1, 2,$$

such that a given mode is unstable if $\Omega_i > 0$, stable if $\Omega_i < 0$ and neutrally stable if $\Omega_i = 0$.[19,23] Here, $\tilde{w}_i$, $\tilde{\eta}_i$, $\tilde{p}$, $\tilde{\pi}$, and $\tilde{h}$ denote the amplitudes of the wall-normal velocity and

vorticity, pressure, second invariant of the rate of strain tensor, and interfacial perturbations, respectively; α and β denote the streamwise and spanwise real wavenumbers, respectively, and $\Omega(=\alpha c)$ stands for the complex disturbance frequency, wherein c is a complex phase speed of the disturbance. This yields the following stability equations in both the layers, following the suppression of the tilde decoration. In the lower layer

$$i\alpha r \, \mathrm{Re}[\{w_1'' - (\alpha^2 + \beta^2)w_1\}(U_1 - c) - U_1''w_1]$$
$$= \mu_1^0[w_1'''' - 2(\alpha^2 + \beta^2)w_1'' + (\alpha^2 + \beta^2)^2 w_1] + 2\mu_1^{0'}[w_1''' - (\alpha^2 + \beta^2)w_1'] + \mu_1^{0''}[w_1'' + (\alpha^2 + \beta^2)w_1]$$
$$- i\alpha U_1'(\mathcal{S}''\pi + 2\mathcal{S}'\pi' + \mathcal{S}\pi'') - 2i\alpha U_1''(\mathcal{S}'\pi + \mathcal{S}\pi') - i\alpha U_1'''\mathcal{S}\pi - i\alpha(\alpha^2 + \beta^2)U_1'\mathcal{S}\pi,$$

(16)

$$ir \, \mathrm{Re}[\alpha\eta_1(U_1 - c) + \beta U_1'w_1]$$
$$= \mu_1^0[\eta_1'' - (\alpha^2 + \beta^2)\eta_1] + \mu_1^{0'}\eta_1'$$
$$+ i\beta U_1'(\mathcal{S}'\pi + \mathcal{S}\pi') + i\beta U_1''\mathcal{S}\pi.$$

(17)

In the upper layer

$$i\alpha \, \mathrm{Re}[\{w_1'' - (\alpha^2 + \beta^2)w_2\}(U_2 - c) - U_2''w_2]$$
$$= w_2'''' - 2(\alpha^2 + \beta^2)w_2'' + (\alpha^2 + \beta^2)^2 w_2,$$

(18)

$$i \, \mathrm{Re}[\alpha\eta_2(U_2 - c) + \beta U_2'w_2] = \eta_2'' - (\alpha^2 + \beta^2)\eta_2.$$

(19)

These equations are then subject to the following boundary conditions: no-slip and no-penetration conditions at the walls can be written as

$$w_1 = w_1' = \eta_1 = 0 \quad \text{at} \ z = 0,$$

(20)

$$w_2 = w_2' = \eta_2 = 0 \quad \text{at} \ z = 1.$$

(21)

The kinematic boundary condition gives

$$h = \frac{w_1}{i\alpha(U_1 - c)} = \frac{w_2}{i\alpha(U_2 - c)}.$$

(22)

Conditions of continuity of the velocity in the streamwise, spanwise and normal directions at the interface are expressed as

$$w_1' - i\alpha h U_1' = w_2' - i\alpha h U_2',$$

(23)

$$\eta_1 + i\beta h U_1' = \eta_2 + i\beta h U_2',$$

(24)

$$w_1 = w_2.$$

(25)

The normal stress jump and continuity of the tangential stress balance in the streamwise and spanwise directions are respectively given by

$$i\alpha \, \mathrm{Re}[r\{w_1'(c - U_1) + U_1'w_1\} - \{w_2'(c - U_2) + U_2'w_2\}]$$
$$- 2\mu_1^0(\alpha^2 + \beta^2)w_1' + 3(\alpha^2 + \beta^2)w_2' + \mu_1^0$$
$$\times [w_1''' - (\alpha^2 + \beta^2)w_1'] + \mu_1^{0'}[w_1'' + (\alpha^2 + \beta^2)w_1]$$
$$- i\alpha[\mathcal{S}U_1'\pi' + \mathcal{S}'U_1'\pi + \mathcal{S}U_1''\pi] - w_2'''$$
$$= (\alpha^2 + \beta^2)\{\Gamma(\alpha^2 + \beta^2) + G\}\frac{(w_2' - w_1')}{i\alpha(U_2' - U_1')},$$

(26)

$$\mu_1^0[w_1'' + (\alpha^2 + \beta^2)w_1] - i\alpha\mathcal{S}U_1'\pi - \frac{(\mu_1^0 U_1'' - U_2'')}{(U_1 - c)}w_1$$
$$= w_2'' + (\alpha^2 + \beta^2)w_2,$$

(27)

$$\mu_1^0\eta_1' + i\beta\mathcal{S}U_1'\pi + \frac{(\mu_1^0 U_1'' - U_2'')}{\alpha(U_1 - c)}\beta w_1 = \eta_2'.$$

(28)

Here, the prime represents differentiation with respect to z, $r \equiv \rho_1/\rho_2$ is the density ratio, $\mathrm{Re}(\equiv\rho U_m H/\mu_2)$ is the Reynolds number, $G \equiv (\rho_1 - \rho_2)gH^2/\mu_2 V$ is a dimensionless gravitational parameter, and $\Gamma \equiv \gamma/\mu_2 V$ is an inverse capillary in which γ denotes the interfacial tension. We have confirmed that Eqs. (16)–(19) along with the boundary conditions (20)–(28) describe an eigenvalue problem that can be recast into the following matrix form:
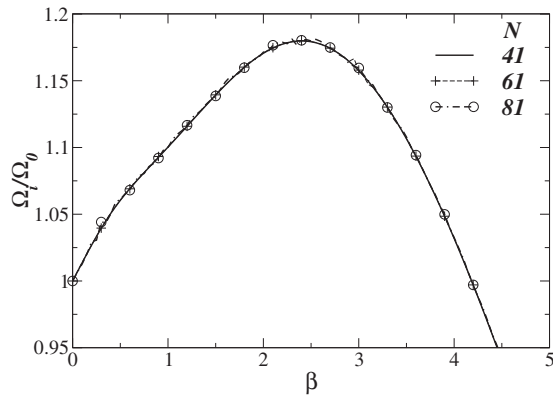
FIG. 3. The effect of increasing the order of Chebyshev polynomials in each layer, N, on the variation of normalized growth rate, (Ω_i/Ω_0), with β, where Ω_0 is the growth rate associated with the corresponding two-dimensional disturbance ($\beta=0$). The rest of the parameter values are Re$=100$, $\Gamma=0.1$, $G=-5$, $m=10$, $r=1.1$, Bn$=4$, $n=1$, $h^0=0.3$, and $\alpha=0.5$.

$$
\begin{bmatrix}
\mathcal{A}_{11} & \mathcal{A}_{12} & \mathcal{A}_{13} & \mathcal{A}_{14} \\
\mathcal{A}_{21} & \mathcal{A}_{22} & \mathcal{A}_{23} & \mathcal{A}_{24} \\
\mathcal{A}_{31} & \mathcal{A}_{32} & \mathcal{A}_{33} & \mathcal{A}_{34} \\
\mathcal{A}_{41} & \mathcal{A}_{42} & \mathcal{A}_{43} & \mathcal{A}_{44}
\end{bmatrix}
\begin{bmatrix}
w_1 \\ w_2 \\ \eta_1 \\ \eta_2
\end{bmatrix}
$$
$$
= c
\begin{bmatrix}
\mathcal{B}_{11} & \mathcal{B}_{12} & \mathcal{B}_{13} & \mathcal{B}_{14} \\
\mathcal{B}_{21} & \mathcal{B}_{22} & \mathcal{B}_{23} & \mathcal{B}_{24} \\
\mathcal{B}_{31} & \mathcal{B}_{32} & \mathcal{B}_{33} & \mathcal{B}_{34} \\
\mathcal{B}_{41} & \mathcal{B}_{42} & \mathcal{B}_{43} & \mathcal{B}_{33}
\end{bmatrix}
\begin{bmatrix}
w_1 \\ w_2 \\ \eta_1 \\ \eta_2
\end{bmatrix},
\tag{29}
$$

where c is the eigenvalue, and (w_1, η_1) and (w_2, η_2) are the eigenfunctions corresponding to the intervals $[0-h^0]$ and $[h^0-1]$, respectively. This eigenvalue problem is then solved using the public domain software, LAPACK, and the Chebyshev spectral collocation method.[24] The above procedure allows the numerical calculation of the dispersion relations $\Omega_i=\Omega_i(\beta;\alpha,\text{Re},m,r,\Gamma,G,n,\text{Bn})$. A similar technique had previously been used by Sahu et al.[14,25]

In the limit $(n,\text{Bn})\rightarrow(1,0)$, we recover the Orr–Sommerfeld and Squire equations for a Newtonian fluid as given in Schmid et al.[23] In the same limit, we also obtained the governing equations of Malik and Hooper[20] for two Newtonian fluids flowing through a channel. By setting $n=1$, we also obtain the stability equations of Nouar et al.[15] for Bingham fluid. By considering two-dimensional disturbances (setting $\beta=0$) and rewriting Eqs. (16) and (28) in terms of stream function, we obtained the corresponding stability equations and boundary conditions of Sahu et al.,[14] although we obtain an extra term in the tangential stress bal-

TABLE I. Maximum normalized growth rate, $(\Omega_i/\Omega_0)_{\text{max}}$ in Fig. 3 for different values of N.

N	$(\Omega_i/\Omega_0)_{\text{max}}$
41	1.179 831 001 1
61	1.180 017 574 2
81	1.180 029 599 6

ance equation in the x-direction, which appears in Eqs. (27) and (28) and is due to the expansion of the streamwise velocity at the perturbed interface.

C. Numerical procedure and validation

In order to inspire confidence in the predictions of the numerical procedure, we investigate the dependence of our numerical solutions upon mesh refinement in Fig. 3 in which we plot the normalized growth rate, Ω_i/Ω_0 with β, where Ω_0, the value of Ω_i associated with two-dimensional disturbance ($\beta=0$) (see Table I for numerical values of the maximum normalized growth rate, $(\Omega_i/\Omega_0)_{\text{max}}$ in Fig. 3 for different values of N). The rest of the parameter values are Re$=100$, $\Gamma=0.1$, $G=-5$, $m=10$, $r=1.1$, Bn$=4$, $n=1$, $\alpha=0.5$, and $h^0=0.3$. It can be seen that the curves are indistinguishable for different values of the order of Chebyshev polynomials, N; $N=61$ is used to generate the rest of the results. Our results are also in excellent agreement with those of Malik and Hooper,[20] South et al.,[10] and Yiantsios and Higgins[5] for two-layer Newtonian flows.

III. RESULTS AND DISCUSSION

In the results discussed below, we reiterate that we have chosen parameters for which there is no Squire's theorem, $h^0/(1-h^0)<\sqrt{m}$, which is guided by the work of Yiantsios and Higgins.[5] We begin the presentation of our results by discussing the behavior of three-dimensional disturbances in pressure-driven channel flow, wherein both the layers are Newtonian fluids, i.e., Bn$=0$ and $n=1$ in the present formulation. We then focus on the so-called "interfacial" modes, before presenting a brief examination of shear modes.

In Figs. 4(a) and 4(b), we show the numerically generated dispersion curves corresponding to the variation of the growth rate, Ω_i, with β for $h^0=0.5$ and $h^0=0.2$, respectively, with α parameterically varying. Here, Ω_i has been normalized by Ω_0 for each value of α used. The rest of the parameter values are Re$=100$, $\Gamma=0$, $G=0$, $m=10$, and $r=1$. As shown in Figs. 4(a) and 4(b), the dispersion curves are paraboloidal for the majority of the α values studied. In Fig. 4(a), it can be seen that these curves exhibit a well-defined maximum at $\beta\approx3.5$ for an intermediate value of α, $\alpha=3$, and "cut-off" modes for which $\Omega_i/\Omega_0<1$ for large β values. Figure 4(b) also shows that the maximal normalized growth rate is associated with a finite β value, and the growth rate increases with decreasing α. Thus, the results depicted in Fig. 4 demonstrate that the linear instabilities accompanying the flow for this set of parameters are three-dimensional. Close inspection of Fig. 4 also reveals that the preferred streamwise wavelength of these instabilities decreases with h^0.

In order to identify the physical mechanism and the nature of unstable modes, we perform an energy budget analysis, similar to that given in Sahu et al.,[14] following the methodology outlined in Appendix B. The energy "budgets" associated with the points labeled A, B, C, D, and E (the maxima in the dispersion curves) in Fig. 4(b) are given in Table II. The figures in Table II represent the contribution
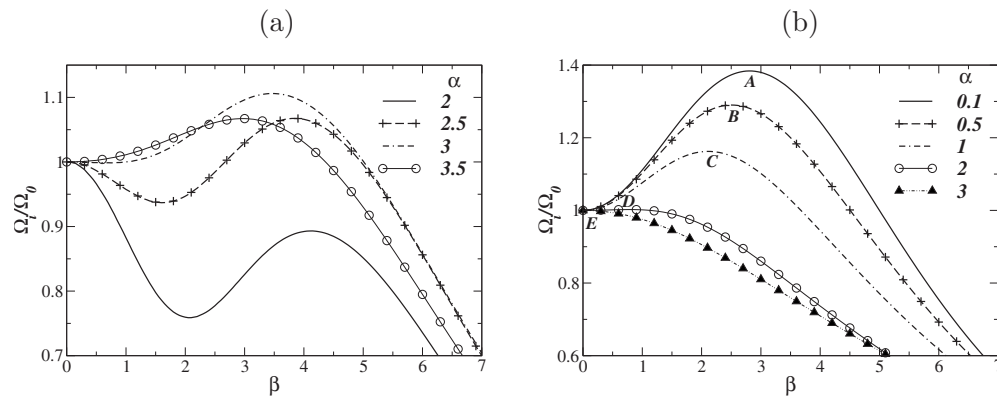
FIG. 4. The dispersion curves (Ω_i/Ω_0 vs β) for different values of α; (a) $h^0=0.5$ and (b) $h^0=0.2$. The rest of the parameter values are Re=100, $\Gamma=0$, $G=0$, $m=10$, $r=1$, Bn=0, and $n=1$. This corresponds to a case where both the layers are Newtonian fluids. The labels $A-E$ in (b) are used to designate the maxima in the dispersion curves; the energy budgets associated with these points are provided in Table II.

arising from each term in Eq. (B1) scaled by the total spatially averaged rate of change of disturbance kinetic energy, KIN.

The energy decomposition reveals that, since TAN_x provides the largest positive contribution to KIN, the unstable modes examined are all of the interfacial type, and, in this case, are driven by viscosity stratification. The other positive, albeit smaller, contribution to KIN for this set of parameters is due to the Reynolds stress in the upper fluid, REY_2. The dissipative terms, DIS_1 and DIS_2 provide negative contributions; this indicates that viscous dissipation provides a restoring effect and is stabilizing, as expected. TAN_y is also negative for intermediate values of α for this set of parameters. It can be seen that although increasing α increases REY_2 for smaller α values, the negative contribution to KIN by the total dissipative energy also increases; hence, overall this has a stabilizing influence. The Reynolds stress term associated with the lower fluid, REY_1, makes a negligible contribution to KIN.

We have also carried out a similar analysis of the flow with $G<0$ for which there is also no Squire's theorem. Our results for this case are illustrated in Figs. 5(a) and 5(b) for $G=-10$ and the rest of the parameters remaining unaltered from Figs. 4(a) and 4(b), respectively; thus, the base flow in this case is unstably stratified. The results presented in Fig. 5 are similar to those presented in Fig. 4 and indicate that this case is also characterized by the presence of three-dimensional instabilities.

In the rest of this paper, we concentrate on studying the effect of three-dimensional disturbances when the lower layer is a Herschel–Bulkley fluid. In Figs. 6(a) and 6(b), we

investigate the effect of varying α values on the dispersion curves (Ω_i/Ω_0 versus β) with Bn=5 for $h^0=0.5$ and $h^0=0.2$, respectively. The rest of the parameter values are the same as those used to generate Fig. 4. It can be seen in Fig. 6(a) that most of these curves exhibit a well-defined maximum at $\beta \approx 3.5$, for an intermediate value of α. The stability behavior of the dispersion curves in Fig. 6(b) is similar to that in Fig. 4(b); the maximum growth rate increases with decreasing α values. We can also see that the value of α associated with the most-dangerous mode is smaller for $h^0=0.2$ as compared to that for $h^0=0.5$.

The dependence of the stability characteristics on α can be explained by inspection of the energy budgets of the points labeled A, B, C, and D in Fig. 6(a), which are listed in Table III. It is seen that the largest contribution to KIN is due to TAN_x, confirming the most dangerous mode to be of interfacial type. It can also be seen that for this set of parameter values, REY_2 increases with increasing α, reaching a maximum for $\alpha \approx 2.5$; a further increase in α values leads to a decrease in REY_2. An opposite effect for the total viscous dissipation energy can be seen in the Table III; REY_1 makes a negligible contribution to KIN. This may provide an explanation for the nonmonotonic dependence on α shown in Fig. 6(a). The energy budgets of the points labeled E, F, G, and H in Fig. 6(b), which are listed in Table IV reveal that although increasing α increases REY_2, the negative contribution to KIN by the total dissipative term DIS also increases. Thus, overall the effect is stabilizing for this set of parameter values.

Next, in Figs. 7(a) and 7(b), we investigate the effect of varying the Bingham number Bn on the three-dimensional

TABLE II. Energy budgets for the points labeled A, B, C, D, and E in Fig. 4(b).

Point	REY_1	REY_2	DIS_1	DIS_2	TAN_x	TAN_y	TEN	HYD
A	0	0.0001	−0.007	−0.1005	1.1075	0	0	0
B	0	0.0066	−0.0077	−0.1	1.1035	−0.0024	0	0
C	0	0.015	−0.0123	−0.0955	1.1015	−0.0087	0	0
D	0	0.0147	−0.032	−0.0761	1.1006	−0.0072	0	0
E	0	0.0148	−0.041	−0.0672	1.0934	0	0	0
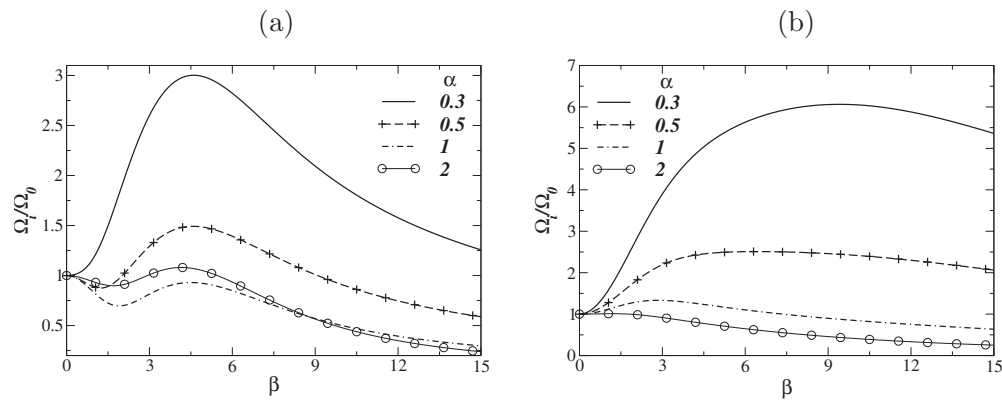
FIG. 5. The dispersion curves (Ω_i/Ω_0 vs β) for different values of α; (a) $h^0=0.5$ and (b) $h^0=0.2$. The rest of the parameter values are the same as in Fig. 4 but with $G=-10$.

linear stability characteristics by showing numerically generated dispersion curves (Ω_i/Ω_0 versus β) for $h^0=0.5$ and $h^0=0.2$, respectively. Here $\alpha=2$ and the rest of the parameter values are the same as those used to generate Fig. 4. It can be seen in Fig. 7(a) that for $h^0=0.5$ the normalized growth rate, Ω_i/Ω_0, increases with increasing Bn, but for $h^0=0.2$, Bn has a nonmonotonic effect on the disturbance growth rate as can be seen in Fig. 7(b). Inspection of Fig. 7(b) reveals that increasing the value of Bn increases Ω_i/Ω_0 in the range $0<\text{Bn}<6$; a further increase in Bn, however, leads to a decrease in the maximal growth rate. Close inspection of Fig. 7(a) also reveals that increasing Bn shifts the most dangerous and cut-off modes toward higher wavenumbers. It can be seen in Figs. 7(a) and 7(b) that for a range of β values considered, $\Omega_i/\Omega_0>1$, thus, linear instabilities accompanying the flow for this set of parameters are three-dimensional.

The energy budgets associated with the points labeled A, B, C, and D, and E, F, G, and H in Figs. 7(a) and 7(b), are listed in Tables V and VI, respectively. For $h^0=0.5$, inspection of Table V reveals that although REY_2 decreases with increasing Bn, the negative contribution provided due to the total viscous dissipation ($\text{DIS}_1+\text{DIS}_2$) increases at a faster rate; TAN_y also increases with increasing Bn. This may explain the destabilizing effect of increasing Bn for $h^0=0.5$. The energy budgets for points E, F, G, and H that are asso-

ciated with $h^0=0.2$ reveals that increasing Bn increases the positive contribution of REY_2 up to $\text{Bn}\approx6$ and decreases thereafter; this trend is consistent with the stability behavior of the dispersion curves in Fig. 7(b). For all h^0 values considered, TAN_x provides the largest positive contribution to KIN, hence the unstable modes examined are all of the interfacial type.

In Fig. 8, we investigate the effect of varying n on the stability characteristics for $\text{Bn}=4$, the rest of the parameters remain unaltered from Fig. 7. For the larger h^0 values examined, decreasing the value of n, which reflects an increase in the shear-thinning tendency of the non-Newtonian layer, has a nonmonotonic effect on the disturbance growth rate. The maximal growth rate decreases with decreasing the value of n; a further decrease in n, however, leads to an increase in the maximal growth rate. In contrast, in Fig. 8(b), which is associated with $h^0=0.2$, we can see that decreasing n increases the maximum growth rate and shifts both the most dangerous and cut-off modes toward larger β values. It can also be seen that $\Omega_i/\Omega_0>1$ for a range of β values for all the values of n (for $h^0=0.2$) and smaller n value (for $h^0=0.5$); thus, three-dimensional instabilities dominate for this set of parameters. The energy budget for Fig. 8 shows the same trends as those associated with Fig. 7.
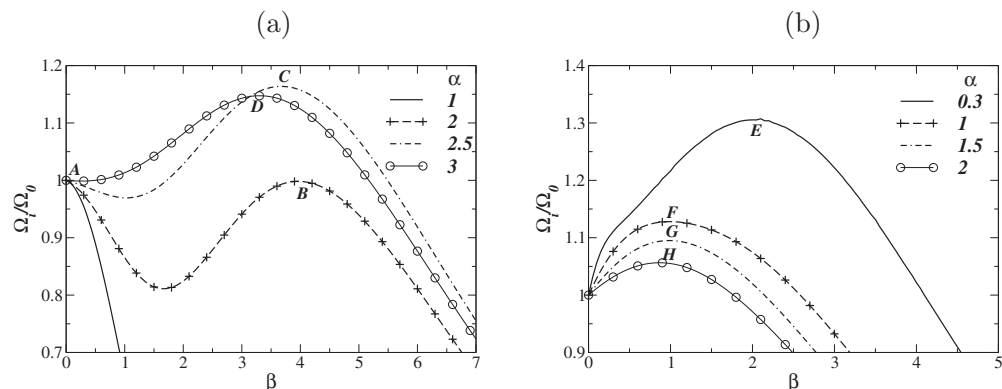
We turn our attention now to a brief examination of

FIG. 6. The dispersion curves (Ω_i/Ω_0 vs β) for different values of α; (a) $h^0=0.5$ and (b) $h^0=0.2$. Here, $\text{Bn}=5$ and the rest of the parameter values are the same as in Fig. 4. The labels $A-D$ and $E-H$ are used to designate maxima in the dispersion curves in (a) and (b), respectively; the energy budgets associated with these points are provided in Tables III and IV, respectively.

TABLE III. Energy budgets for the points labeled A, B, C, and D in Fig. 6(a).

Point	REY_1	REY_2	DIS_1	DIS_2	TAN_x	TAN_y	TEN	HYD
A	−0.0001	0.0188	−0.0619	−0.0458	1.089	0	0	0
B	−0.0002	0.0219	−0.0335	−0.0479	1.0534	0.0063	0	0
C	−0.0003	0.0238	−0.032	−0.0457	1.0475	0.0067	0	0
D	−0.0003	0.0147	−0.0369	−0.0431	1.0598	0.0058	0	0

shear modes, which arise at sufficiently large Re. In Figs. 9(a) and 9(b), we show the parametric dependence of the neutral stability curves on the spanwise wavenumber β for the case of Newtonian fluids. Here, Re has been chosen to be sufficiently large so that an additional unstable mode exists, the so-called shear mode; examples of the z-dependence of the stream function associated with the interfacial and shear modes are shown in Figs. 9(c) and 9(d). As can be seen in Figs. 9(a) and 9(b), the most unstable shear modes correspond to two-dimensional perturbations for both values of values of h^0 investigated: increasing β above $\beta=0$ leads to an increase in the value of the critical Re. In Figs. 9(e) and 9(f), it is seen that the growth rates of the interfacial modes far exceed those of the shear ones; the former are also largely insensitive to β variations.

We have also examined the effect of β on the stability of the flow to shear modes with $Bn>0$ and $n\neq1$. In Figs. 10(a), 10(c), and 10(e), we show that increasing the value of β increases the critical Re for shear mode instabilities for all Bn values investigated. A similar result is obtained for n variations, as shown in Figs. 10(b), 10(d), and 10(f). Collectively, the results presented in Fig. 10 demonstrate that two-dimensional shear modes are more linearly unstable than their three-dimensional counterparts for situations wherein the lower layer is non-Newtonian. We have also found similar results for other parameters for which Squire's theorem does not exist (e.g., for $G<0$ and $h^0=0.2$); these have been omitted for brevity.

IV. CONCLUSIONS

We have investigated the three-dimensional linear characteristics of pressure-driven two-layer channel flow wherein a Newtonian layer flows past a Herschel–Bulkley fluid. We have restricted attention to the range of parameters over which Squire's theorem for the Newtonian two-layer problem does not exist. In order to examine the stability characteristics of the flow, we have derived modified Orr–Sommerfeld and Squire equations in each layer, which constitute an eigenvalue problem. These equations are parameterized by a Bingham number, Bn, and a flow index, n, in addition to viscosity, density and thickness ratios, and gravitational and interfacial tension parameters. The eigenvalue problem is then solved using an efficient spectral collocation method.

Our results indicate the presence of three-dimensional instabilities for situations where the square root of the viscosity ratio is larger than the thickness ratio of the two layers; these instabilities are also present when density stratification is destabilizing. In all cases studied, an energy "budget" analysis shows that the most dangerous modes are interfacial ones. These results may be of particular interest to researchers studying the transient growth of the disturbances and their nonlinear evolution in two-fluid flows. Our brief examination of shear mode instabilities, which are present at sufficiently large Reynolds numbers, has also demonstrated that the two-dimensional modes are more unstable than the three-dimensional ones for all the cases studied.

APPENDIX A: DERIVATION OF THE LINEAR STABILITY EQUATIONS

In this appendix, we include details of the derivation of the linear stability equations. First, we derive the stability equations for the non-Newtonian layer; we then use the appropriate limits to derive the equations for the Newtonian layer. We follow the procedure given in Ref. 23 in deriving the following stability equations.

TABLE IV. Energy budgets for the points labeled E, F, G, and H in Fig. 6(b).

Point	REY_1	REY_2	DIS_1	DIS_2	TAN_x	TAN_y	TEN	HYD
E	0	0.0004	−0.025	−0.0395	1.0642	−0.0001	0	0
F	0	0.0052	−0.0333	−0.0369	1.0703	−0.0052	0	0
G	0	0.0063	−0.0376	−0.0335	1.07	−0.0052	0	0
H	0	0.0059	−0.0428	−0.0304	1.0708	−0.0034	0	0
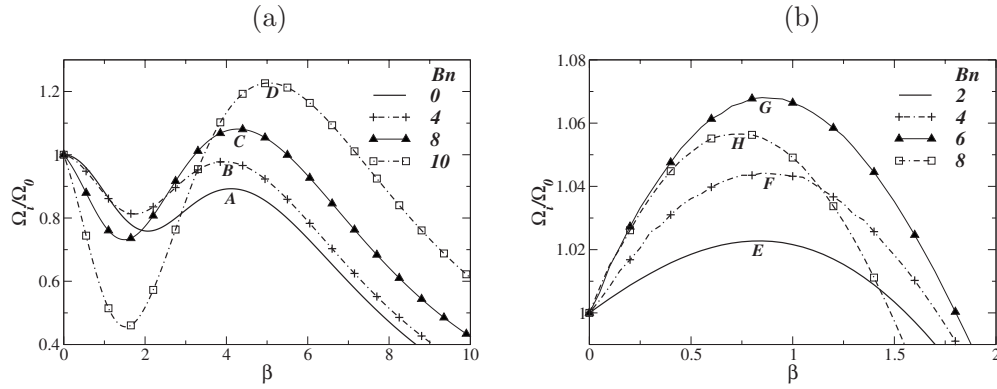
FIG. 7. The dispersion curves (Ω_i/Ω_0 vs β) for different values of Bn; (a) $h^0 = 0.5$ and (b) $h^0 = 0.2$. Here, $\alpha = 2$ and the rest of the parameter values are the same as in Fig. 4. The labels $A-D$ and $E-H$ are used to designate maxima in the dispersion curves in (a) and (b), respectively; the energy budgets associated with these points are provided in Tables V and VI, respectively.

Step 1: The mass and momentum conservation equations.

$$
r\left[\frac{\partial u}{\partial t} + u\frac{\partial u}{\partial x} + v\frac{\partial u}{\partial y} + w\frac{\partial u}{\partial z}\right]
$$
$$
= -\frac{1}{Re}\frac{\partial p}{\partial x} + \frac{1}{Re}\left[\frac{\partial}{\partial x}\left(2\mu\frac{\partial u}{\partial x}\right) + \frac{\partial}{\partial y}\left\{\mu\left(\frac{\partial u}{\partial y} + \frac{\partial v}{\partial x}\right)\right\}\right.
$$
$$
\left. + \frac{\partial}{\partial z}\left\{\mu\left(\frac{\partial w}{\partial x} + \frac{\partial u}{\partial z}\right)\right\}\right], \tag{A1}
$$

$$
r\left[\frac{\partial v}{\partial t} + u\frac{\partial v}{\partial x} + v\frac{\partial v}{\partial y} + w\frac{\partial v}{\partial z}\right]
$$
$$
= -\frac{1}{Re}\frac{\partial p}{\partial y} + \frac{1}{Re}\left[\frac{\partial}{\partial x}\left\{\mu\left(\frac{\partial v}{\partial x} + \frac{\partial u}{\partial y}\right)\right\} + \frac{\partial}{\partial y}\left(2\mu\frac{\partial v}{\partial y}\right)\right.
$$
$$
\left. + \frac{\partial}{\partial z}\left\{\mu\left(\frac{\partial v}{\partial z} + \frac{\partial w}{\partial y}\right)\right\}\right], \tag{A2}
$$

$$
r\left[\frac{\partial w}{\partial t} + u\frac{\partial w}{\partial x} + v\frac{\partial w}{\partial y} + w\frac{\partial w}{\partial z}\right]
$$
$$
= -\frac{1}{Re}\frac{\partial p}{\partial z} + \frac{1}{Re}\left[\frac{\partial}{\partial x}\left\{\mu\left(\frac{\partial w}{\partial x} + \frac{\partial u}{\partial z}\right)\right\}\right.
$$
$$
\left. + \frac{\partial}{\partial y}\left\{\mu\left(\frac{\partial v}{\partial z} + \frac{\partial w}{\partial y}\right)\right\} + \frac{\partial}{\partial z}\left(2\mu\frac{\partial w}{\partial z}\right)\right], \tag{A3}
$$

$$
\frac{\partial u}{\partial x} + \frac{\partial v}{\partial y} + \frac{\partial w}{\partial z} = 0. \tag{A4}
$$

Here the viscosity, μ_1, is modeled as a Herschel–Bulkley fluid

$$
\mu_1 = m\pi^{n-1} + Bn\pi^{-1}, \tag{A5}
$$

where π is the second invariant of strain-rate tensor given by

$$
\pi = [2\{E_{xx}^2 + E_{yy}^2 + E_{zz}^2 + 2(E_{xy}^2 + E_{yz}^2 + E_{xz}^2)\}]^{1/2}, \tag{A6}
$$

and E_{ij} is defined as

$$
E_{ij} = \frac{1}{2}\left(\frac{\partial u_i}{\partial x_j} + \frac{\partial u_j}{\partial x_i}\right), \quad (i,j = x,y,z).
$$

Step 2: Each variable is expressed as the sum of a base state and a 3D perturbation.

$$
u = U + \hat{u}, \quad v = V + \hat{v}, \quad w = W + \hat{w}, \quad p = P + \hat{p}, \tag{A7}
$$

$$
\mu_1(\pi) = \mu_1^0 + \left.\frac{\partial\mu_1}{\partial\pi}\right|^0 (\pi - \Pi) \equiv \mu_1^0 + \mathcal{S}\hat{\pi} \equiv \mu_1^0 + \hat{\mu}, \tag{A8}
$$

$$
h(x,y,t) = h^0 + \hat{h}, \tag{A9}
$$

TABLE V. Energy budgets for the points labeled A, B, C, and D in Fig. 7(a).

Point	REY$_1$	REY$_2$	DIS$_1$	DIS$_2$	TAN$_x$	TAN$_y$	TEN	HYD
A	-0.0004	0.0193	-0.0139	-0.0995	1.0938	0.0006	0	0
B	-0.0003	0.0136	-0.0201	-0.0575	1.0595	0.0047	0	0
C	-0.0002	0.0073	-0.0413	-0.0268	1.0483	0.0126	0	0
D	-0.0001	0.0042	-0.0523	-0.0146	1.1636	0.0193	0	0

TABLE VI. Energy budgets for the points labeled E, F, G, and H in Fig. 7(b).

Point	REY$_1$	REY$_2$	DIS$_1$	DIS$_2$	TAN$_x$	TAN$_y$	TEN	HYD
E	0	0.012	-0.0324	-0.0585	1.0854	-0.0064	0	0
F	0	0.0081	-0.0326	-0.04	1.069	-0.0046	0	0
G	0	0.0093	-0.0284	-0.0231	1.0541	-0.0019	0	0
H	0	0.0012	-0.057	-0.0073	1.0601	0.0031	0	0

where $\mathcal{S} \equiv \partial \mu_1 / \partial \pi |^0 = (n-1)m\Pi^{n-2} - \mathrm{Bn}\Pi^{-2}$. The base state viscosity, μ_1^0 is given by

$$\mu_1^0 = m\Pi^{n-1} + \mathrm{Bn}\Pi^{-1}, \qquad (A10)$$

where $\Pi \equiv \partial U / \partial z$ (fully developed state). The linearized form of $\hat{\pi}$ is given by

$$\hat{\pi} = \left(\frac{\partial \hat{u}}{\partial z} + \frac{\partial \hat{w}}{\partial x} \right). \qquad (A11)$$

Now performing the following steps.

(i) Substituting Eqs. (A7)–(A10) into Eqs. (A1)–(A4).
(ii) Subtracting the base state equations.
(iii) Linearizing the resultant equations, we get

$$r \left[\frac{\partial \hat{u}}{\partial t} + U \frac{\partial \hat{u}}{\partial x} + \hat{w} U' \right]$$
$$= -\frac{1}{\mathrm{Re}} \frac{\partial \hat{p}}{\partial x} + \frac{1}{\mathrm{Re}} \left[\mu_0 \left(\frac{\partial^2 \hat{u}}{\partial x^2} + \frac{\partial^2 \hat{u}}{\partial y^2} + \frac{\partial^2 \hat{u}}{\partial z^2} \right) \right.$$
$$\left. + \mu_0' \frac{\partial \hat{w}}{\partial x} + \mu_0' \frac{\partial \hat{u}}{\partial z} + U' \frac{\partial \hat{\mu}}{\partial z} + U'' \hat{\mu} \right], \qquad (A12)$$

$$r \left[\frac{\partial \hat{v}}{\partial t} + U \frac{\partial \hat{v}}{\partial x} \right] = -\frac{1}{\mathrm{Re}} \frac{\partial \hat{p}}{\partial y} + \frac{1}{\mathrm{Re}} \left[\mu_0 \left(\frac{\partial^2 \hat{v}}{\partial x^2} + \frac{\partial^2 \hat{v}}{\partial y^2} \right. \right.$$
$$\left. \left. + \frac{\partial^2 \hat{v}}{\partial z^2} \right) + \mu_0' \frac{\partial \hat{v}}{\partial z} + \mu_0' \frac{\partial \hat{w}}{\partial y} \right], \qquad (A13)$$

$$r \left[\frac{\partial \hat{w}}{\partial t} + U \frac{\partial \hat{w}}{\partial x} \right] = -\frac{1}{\mathrm{Re}} \frac{\partial \hat{p}}{\partial z} + \frac{1}{\mathrm{Re}} \left[\mu_0 \left(\frac{\partial^2 \hat{w}}{\partial x^2} + \frac{\partial^2 \hat{w}}{\partial y^2} \right. \right.$$
$$\left. \left. + \frac{\partial^2 \hat{w}}{\partial z^2} \right) + U' \frac{\partial \hat{\mu}}{\partial x} + 2\mu_0' \frac{\partial \hat{w}}{\partial z} \right], \qquad (A14)$$

$$\frac{\partial \hat{u}}{\partial x} + \frac{\partial \hat{v}}{\partial y} + \frac{\partial \hat{w}}{\partial z} = 0. \qquad (A15)$$

Step 3:

$$\frac{\partial}{\partial x}(\mathrm{Eq.A12}) + \frac{\partial}{\partial y}(\mathrm{Eq.A13}) + \frac{\partial}{\partial z}(\mathrm{Eq.A14}) \Rightarrow \frac{1}{\mathrm{Re}}\nabla^2 \hat{p}$$
$$= -2U'r \frac{\partial \hat{w}}{\partial x} + \frac{1}{\mathrm{Re}} \left[2\mu_0' \nabla^2 \hat{w} + 2U' \frac{\partial^2 \hat{\mu}}{\partial x \, \partial z} \right.$$
$$\left. + 2U'' \frac{\partial \hat{\mu}}{\partial x} + 2\mu_0'' \frac{\partial \hat{w}}{\partial z} \right]. \qquad (A16)$$
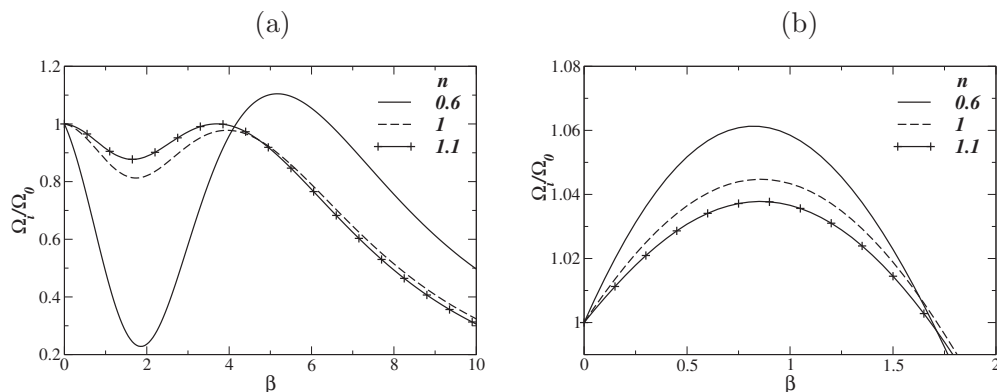
Step 4:

(a)

(b)

FIG. 8. The dispersion curves (Ω_i/Ω_0 vs β) for different values of n; (a) $h^0 = 0.5$ and (b) $h^0 = 0.2$. Here, Bn$=4$ and the rest of the parameter values are the same as in Fig. 7.
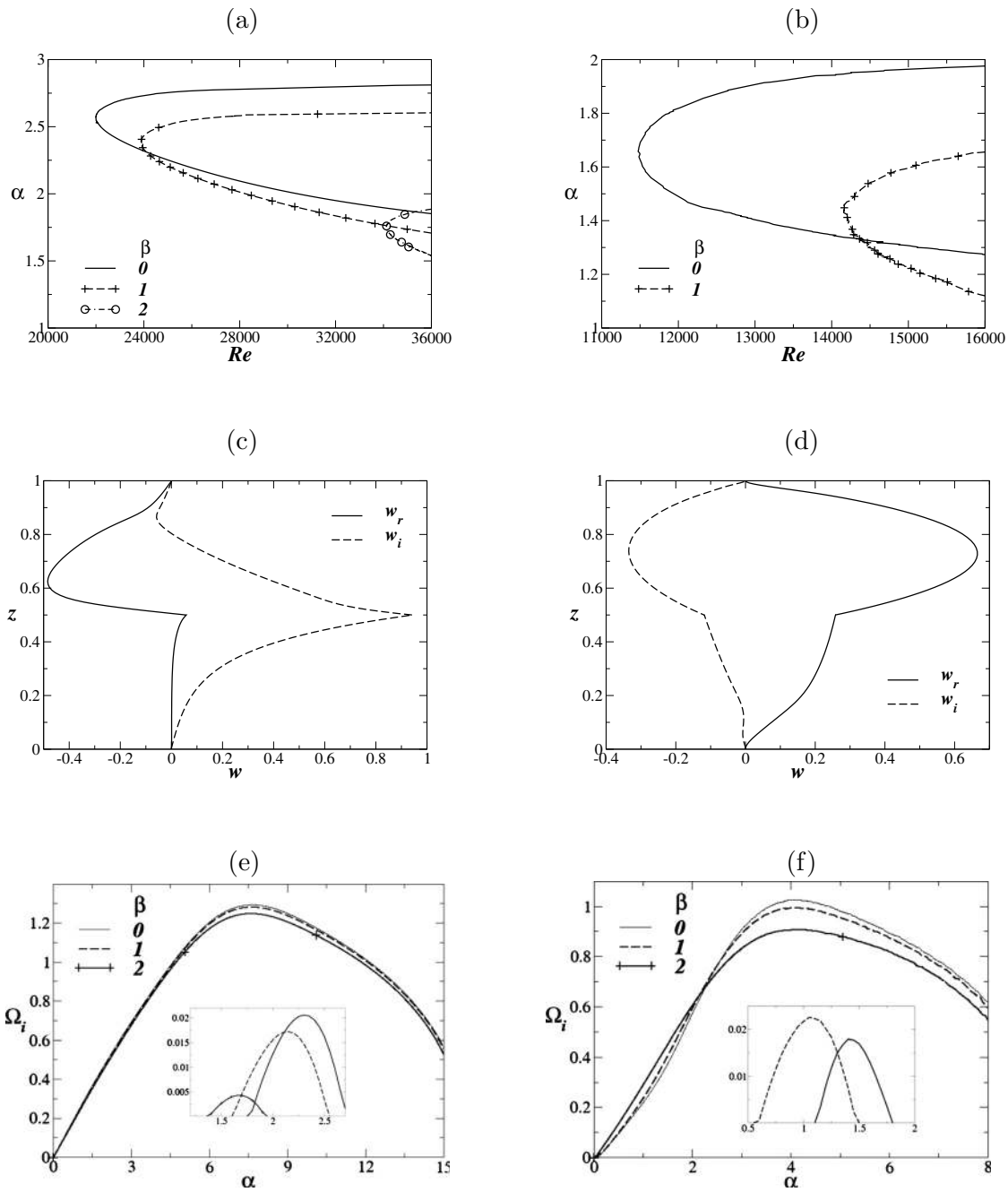
FIG. 9. The effect of varying β on the neutral stability curves of the shear mode, (a) and (b), the cross-stream structure of the real and imaginary parts of ψ associated with the most dangerous interfacial and shear modes in panel (e) are shown in panels (c) and (d); the dispersion curves (Ω_i vs α) are shown in panels (e) and (f). Panels (a), (c), and (e), and (b), (d), and (f) are associated with $h^0=0.5$ and $h^0=0.2$, respectively. The rest of the parameter values are Re=40 000, Bn=0, $n=1$, $m=10$, $r=1$, $G=0$, and $\Gamma=1$.

$$\frac{\partial^2}{\partial x^2}(\text{Eq.A14}) + \frac{\partial^2}{\partial y^2}(\text{Eq.A14}) + \frac{\partial^2}{\partial z^2}(\text{Eq.A14})$$

$$\Rightarrow r\left[\frac{\partial}{\partial t}(\nabla^2\hat{w}) + U\frac{\partial}{\partial x}(\nabla^2\hat{w}) + U''\frac{\partial\hat{w}}{\partial x} + 2U'\frac{\partial^2\hat{w}}{\partial x\,\partial z} \right]$$

$$= -\frac{1}{\text{Re}}\frac{\partial}{\partial z}(\nabla^2\hat{p}) + \frac{1}{\text{Re}}\left[\mu_0\frac{\partial^2}{\partial x^2}(\nabla^2\hat{w}) + \mu_0\frac{\partial^2}{\partial y^2}(\nabla^2\hat{w}) + \mu_0\frac{\partial^2}{\partial z^2}(\nabla^2\hat{w}) + 4\mu_0'\frac{\partial}{\partial z}(\nabla^2\hat{w}) + \mu_0''(\nabla^2\hat{w}) \right.$$

$$\left. + U'\frac{\partial^3\hat{\mu}}{\partial x^3} + U'\frac{\partial^3\hat{\mu}}{\partial x\,\partial y^2} + U'\frac{\partial^3\hat{\mu}}{\partial x\,\partial z^2} + 2U''\frac{\partial^2\hat{\mu}}{\partial x\,\partial z} + U'''\frac{\partial\hat{\mu}}{\partial x} + 4\mu_0''\frac{\partial^2\hat{w}}{\partial z^2} + 2\mu_0'''\frac{\partial\hat{w}}{\partial z} \right]. \tag{A17}$$

Step 5: Differentiating Eq. (A16) with respect to z and substituting the resultant equations into Eq. (A17), we obtain

$$r\left[\frac{\partial}{\partial t}(\nabla^2 \hat{w}) + U\frac{\partial}{\partial x}(\nabla^2 \hat{w}) - U''\frac{\partial \hat{w}}{\partial x}\right]$$

$$= \frac{1}{\text{Re}}\left[\mu_0 \frac{\partial^2}{\partial x^2}(\nabla^2 \hat{w}) + \mu_0 \frac{\partial^2}{\partial y^2}(\nabla^2 \hat{w}) + \mu_0 \frac{\partial^2}{\partial z^2}(\nabla^2 \hat{w})\right.$$

$$+ 2\mu_0'\frac{\partial}{\partial z}(\nabla^2 \hat{w}) - \mu_0''(\nabla^2 \hat{w}) - U'\frac{\partial^3 \hat{\mu}}{\partial x \partial z^2}$$

$$- 2U''\frac{\partial^2 \hat{\mu}}{\partial x \partial z} - U'''\frac{\partial \hat{\mu}}{\partial x} + U'\frac{\partial^3 \hat{\mu}}{\partial x^3}$$

$$\left. + U'\frac{\partial^3 \hat{\mu}}{\partial x \partial y^2} + 2\mu_0''\frac{\partial^2 \hat{w}}{\partial z^2}\right] \tag{A18}$$

Step 6:

$$\frac{\partial}{\partial y}(\text{Eq.A12}) - \frac{\partial}{\partial x}(\text{Eq.A13})$$

$$\Rightarrow r\left[\frac{\partial \hat{\eta}}{\partial t} + U\frac{\partial \hat{\eta}}{\partial x} + U'\frac{\partial \hat{w}}{\partial y}\right]$$

$$= \frac{1}{\text{Re}}\left[\mu_0(\nabla^2 \hat{\eta}) + \mu_0'\frac{\partial \hat{\eta}}{\partial z} + U'\frac{\partial^2 \hat{\mu}}{\partial y \partial z} + U''\frac{\partial \hat{\mu}}{\partial y}\right], \tag{A19}$$

where

$$\hat{\eta} = \frac{\partial \hat{u}}{\partial y} - \frac{\partial \hat{v}}{\partial x}.$$

Equations (A18) and (A19) are then decomposed into an amplitude and a wave part by using a normal modes analysis

$$(\hat{w}, \hat{\eta}, \hat{p}, \hat{\pi})(x,y,z,t) = (w, \eta, p, \pi)(z)x e^{\mathbf{i}(\alpha x + \beta y - \Omega t)},$$

$$\hat{h}(x,y,t) = h e^{i(\alpha x + \beta y - \Omega t)}. \tag{A20}$$

This yields the following stability equations for the Herschel–Bulkley layer:

$$\mathbf{i}\alpha r \, \text{Re}[\{w_1'' - (\alpha^2 + \beta^2)w_1\}(U - c) - U''w_1]$$

$$= \mu_1^0[w_1'''' - 2(\alpha^2 + \beta^2)w_1'' + (\alpha^2 + \beta^2)^2 w_1] + 2\mu_1^{0'}[w_1''' - (\alpha^2 + \beta^2)w_1'] + \mu_1^{0''}[w_1'' + (\alpha^2 + \beta^2)w_1]$$

$$- \mathbf{i}\alpha U'(\mathcal{S}''\pi + 2\mathcal{S}'\pi' + \mathcal{S}\pi'') - 2\mathbf{i}\alpha U''(\mathcal{S}'\pi + \mathcal{S}\pi') - \mathbf{i}\alpha U'''\mathcal{S}\pi - \mathbf{i}\alpha(\alpha^2 + \beta^2)U'\mathcal{S}\pi, \tag{A21}$$

$$\mathbf{i}r \, \text{Re}[\alpha\eta_1(U - c) + \beta U' w_1]$$

$$= \mu_1^0[\eta_1'' - (\alpha^2 + \beta^2)\eta_1] + \mu_1^{0'}\eta_1'$$

$$+ \mathbf{i}\beta U'(\mathcal{S}'\pi + \mathcal{S}\pi') + \mathbf{i}\beta U''\mathcal{S}\pi. \tag{A22}$$

By setting $n = 1$, we recover the stability equations of Nouar *et al.*[15,21] for a Bingham fluid. In the limit $(n, \text{Bn}) \to (1, 0)$, we recover the Orr–Sommerfeld and Squire equations for a Newtonian fluid as given in Schmid *et al.*[23]

APPENDIX B: ENERGY METHOD

Here we have carried out an "energy" budget analysis as given in Refs. 13 and 26. Decomposition of the energy equation into energy production and dissipation terms allows one to isolate the mechanisms by which energy is transferred from the base flow to the disturbances. This decomposition also allows one to determine the type of instability mode, whether interfacial or shear. A similar analysis was also performed recently by Sahu *et al.*[14,27] and Selvam *et al.*[28] for immiscible non-Newtonian, miscible channel flows and miscible core annular flows, respectively. The energy equation is derived by taking the inner product of the horizontal and vertical components of the Navier–Stokes equations with their respective velocity components. The resultant equation

is then averaged over the wavelengths, $2\pi/\alpha$ and $2\pi/\beta$, in the x and y directions, respectively, and integrated over the height of channel:

$$\sum_{j=1}^{2} \text{KIN}_j = \sum_{j=1}^{2} \text{DIS}_j + \sum_{j=1}^{2} \text{REY}_j + \text{INT}, \tag{B1}$$

where subscript $j = 1$ and $j = 2$ represent the lower (non-Newtonian) and upper (Newtonian) fluids, respectively. In Eq. (B1), KIN_j, DIS_j, and REY_j are expressed by

$$\text{KIN}_j = \frac{r_j}{\lambda_1 \lambda_2} \frac{d}{dt} \int_{a_j}^{b_j} dz \int_0^{\lambda_2} dy \int_0^{\lambda_1} dx \left[\frac{1}{2}(\hat{u}_j^2 + \hat{v}_j^2 + \hat{w}_j^2)\right], \tag{B2}$$

$$\text{DIS}_j = -\frac{1}{\lambda_1 \lambda_2 \, \text{Re}} \int_{a_j}^{b_j} dz \int_0^{\lambda_2} dy \int_0^{\lambda_1} \mu_j dx$$

$$\times \left[2\left(\frac{\partial \hat{u}_j}{\partial x}\right)^2 + 2\left(\frac{\partial \hat{v}_j}{\partial y}\right)^2 + 2\left(\frac{\partial \hat{w}_j}{\partial z}\right)^2\right.$$

$$\left. + \left(\frac{\partial \hat{u}_j}{\partial z} + \frac{\partial \hat{w}_j}{\partial x}\right)^2 + \left(\frac{\partial \hat{u}_j}{\partial y} + \frac{\partial \hat{v}_j}{\partial x}\right)^2 + \left(\frac{\partial \hat{v}_j}{\partial z} + \frac{\partial \hat{w}_j}{\partial y}\right)^2\right], \tag{B3}$$
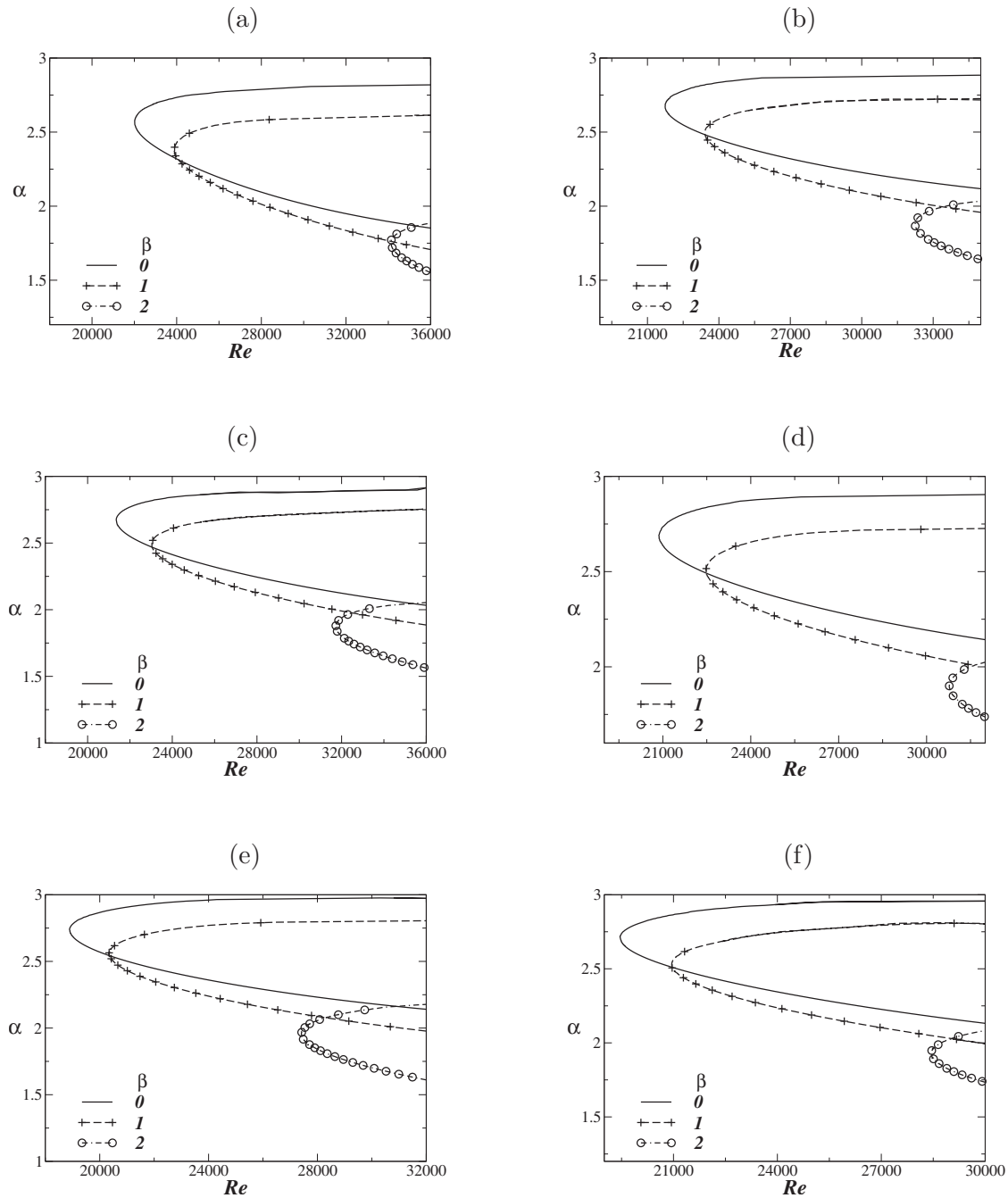
FIG. 10. The effect of varying β on the neutral stability curves of the shear mode Bn=0 (a), Bn=4 (c), Bn=8 (e), n=0.95 (b), n=1 (d), and n=1.1 (f). The rest of the parameter values in the panels are Re=30 000, Bn=5, n=1, m=10, h^0=0.5, r=1, G=0, and Γ=1.

$$\text{REY}_j = \frac{r_j}{\lambda_1 \lambda_2} \int_{a_j}^{b_j} dz \int_0^{\lambda_2} dy \int_0^{\lambda_1} dx \left[-\hat{u}_j \hat{w}_j \frac{\partial U_j}{\partial z} \right], \quad \text{(B4)}$$

for the lower fluid, $\mu_1 = m\Pi^{n-1} + \text{Bn}\Pi^{-1}$, $r_1 = r$, $a_1 = 0$, $b_1 = h$, and for the upper fluid, $\mu_2 = 1$, $r_2 = 1$, $a_2 = h$, and $b_2 = 1$. KIN_j represents the spatially averaged rate of change of disturbance kinetic energy and is proportional to the growth rate. DIS_j represents the viscous dissipation of energy and is always negative; note the presence of μ_1 inside the integrand for the non-Newtonian fluid. INT=NOR+TAN is associated with the existence of an interface and is decomposed into NOR and TAN, the work done by the velocity and stress

disturbances in the directions normal and tangential to the interface, respectively. NOR is given by

$$\text{NOR} = \frac{1}{\lambda_1 \lambda_2 \, \text{Re}} \int_0^{\lambda_2} dy \int_0^{\lambda_1} dx [\hat{w}_1 \tau_1^{zz} - \hat{w}_2 \tau_2^{zz}]_h^0, \quad \text{(B5)}$$

which is further decomposed into TEN and HYD, work done against the deformation of the interface due to interfacial tension and gravity, respectively

$$\text{NOR} \equiv \text{TEN} + \text{HYD}, \quad \text{(B6)}$$

where

$$\mathrm{TEN} = \frac{1}{\lambda_1 \lambda_2 \, \mathrm{Re}} \int_0^{\lambda_2} dy \int_0^{\lambda_1} dx [\hat{w} \Gamma (\hat{h}_{xx} + \hat{h}_{yy})]_{z=h}, \qquad \text{(B7)}$$

and

$$\mathrm{HYD} = \frac{1}{\lambda_1 \lambda_2 \, \mathrm{Re}} \int_0^{\lambda_2} dy \int_0^{\lambda_1} dx [\hat{w} G \hat{h}]_{z=h}. \qquad \text{(B8)}$$

TAN is also further decomposed into TAN_x and TAN_y, work done by the velocity and stress disturbances in the streamwise and spanwise directions, respectively

$$\mathrm{TAN}_x = \frac{1}{\lambda_1 \lambda_2 \, \mathrm{Re}} \int_0^{\lambda_2} dy \int_0^{\lambda_1} dx [\hat{u}_1 \tau_1^{xz} - \hat{u}_2 \tau_2^{xz}]_h, \qquad \text{(B9)}$$

$$\mathrm{TAN}_y = \frac{1}{\lambda_1 \lambda_2 \, \mathrm{Re}} \int_0^{\lambda_2} dy \int_0^{\lambda_1} dx [\hat{v}_1 \tau_1^{yz} - \hat{v}_2 \tau_2^{yz}]_h. \qquad \text{(B10)}$$

In Eqs. (B5), (B9), and (B10) the components of stress tensor are defined as

$$\tau_j^{xz} = \mu_j \left(\frac{\partial \hat{u}_j}{\partial z} + \frac{\partial \hat{w}_j}{\partial x} \right), \quad \tau_j^{yz} = \mu_j \left(\frac{\partial \hat{v}_j}{\partial z} + \frac{\partial \hat{w}_j}{\partial y} \right),$$

$$\text{(B11)}$$

$$\text{and} \quad \tau_j^{zz} = -\hat{p}_j + 2\mu_j \frac{\partial \hat{w}_j}{\partial z},$$

where p_j denote the pressure disturbances.

[1] D. D. Joseph, R. Bai, K. P. Chen, and Y. Y. Renardy, "Core-annular flows," Annu. Rev. Fluid Mech. **29**, 65 (1997).

[2] Q. Cao, L. Ventresca, K. R. Sreenivas, and A. K. Prasad, "Instability due to viscosity stratification downstream of a centreline injector," Can. J. Chem. Eng. **81**, 913 (2003).

[3] M. Regner, M. Henningsson, J. Wiklund, K. Östergren, and C. Trägårdh, "Predicting the displacement of yoghurt by water in a pipe using CFD," Chem. Eng. Technol. **30**, 844 (2007).

[4] C. S. Yih, "Instability due to viscous stratification," J. Fluid Mech. **27**, 337 (1967).

[5] S. G. Yiantsios and B. G. Higgins, "Linear stability of plane Poiseuille flow of two superposed fluids," Phys. Fluids **31**, 3225 (1988).

[6] B. Khomami, "Interfacial stability and deformation of two stratified power-law fluids in plane Poisuille flow. Part I. Stability analysis," J. Non-Newtonian Fluid Mech. **36**, 289 (1990).

[7] B. Khomami, "Interfacial stability and deformation of two stratified power-law fluids in plane Poisuille flow. Part II. Interface deformation," J. Non-Newtonian Fluid Mech. **37**, 19 (1990).

[8] S. G. Yiantsios and B. G. Higgins, "Numerial solution of eigenvalue problems using the compound matrix-method," J. Comput. Phys. **74**, 25 (1988).

[9] A. P. Hooper and W. G. C. Boyd, "Shear flow instability at the interface between two fluids," J. Fluid Mech. **128**, 507 (1983).

[10] M. J. South and A. P. Hooper, "Linear growth in two-fluid plane Poiseuille flow," J. Fluid Mech. **381**, 121 (1999).

[11] I. A. Frigaard, "Super-stable parallel flows of multiple visco-plastic fluids," J. Non-Newtonian Fluid Mech. **100**, 49 (2001).

[12] T. W. Kao and C. Park, "Experimental investigations of the stability of channel flows. Part 2. Two-layered co-current flow in a rectangular channel," J. Fluid Mech. **52**, 401 (1972).

[13] P. A. M. Boomkamp and R. H. M. Miesen, "Classification of instabilities in parallel two-phase flow," Int. J. Multiphase Flow **22**, 67 (1996).

[14] K. C. Sahu, P. Valluri, P. D. M. Spelt, and O. K. Matar, "Linear instability of pressure-driven channel flow of a Newtonian and Herschel-Bulkley fluid," Phys. Fluids **19**, 122101 (2007).

[15] C. Nouar, N. Kabouya, J. Dusek, and M. Mamou, "Modal and non-modal linear stability of the plane Bingham–Poiseuille flow," J. Fluid Mech. **577**, 211 (2007).

[16] I. A. Frigaard, S. D. Howison, and I. J. Sobey, "On the stability of Poiseuille flow of a Bingham fluid," J. Fluid Mech. **263**, 133 (1994).

[17] A. Pinarbasi and A. Liakopoulos, "Stability of two-layer Poiseulle flow of Carreau-Yasuda and Bingham-like fluids," J. Non-Newtonian Fluid Mech. **57**, 227 (1995).

[18] H. B. Squire, "On the stability for three-dimensional disturbances of viscous fluid flow between parallel walls," Proc. R. Soc. London, Ser. A **142**, 621 (1933).

[19] P. G. Drazin and W. H. Reid, *Hydrodynamic Stability* (Cambridge University Press, Cambridge, 1985).

[20] S. V. Malik and A. P. Hooper, "Three-dimensional disturbances in channel flows," Phys. Fluids **19**, 052102 (2007).

[21] I. Frigaard and C. Nouar, "On three-dimensional linear stability of Poiseuille flow of Bingham fluids," Phys. Fluids **15**, 2843 (2003).

[22] C. Nouar and A. Bottaro, "Stability of the flow of a Bingham fluid in a channel: eigenvalue sensitivity, minimal defects and scaling laws of transition," J. Fluid Mech. **642**, 349 (2010).

[23] P. J. Schmid and D. S. Henningson, *Stability and Transition in Shear Flows* (Springer, New York, 2001).

[24] C. Canuto, M. Y. Hussaini, A. Quarteroni, and T. Zang, *Spectral Methods in Fluid Dynamics*, 1st ed. (Springer-Verlag, Amsterdam, 1987), pp. 65–70.

[25] K. C. Sahu and R. Govindarajan, "Stability of flow through a slowly diverging pipe," J. Fluid Mech. **531**, 325 (2005).

[26] R. Govindarajan, S. V. L'vov, and I. Procaccia, "Retardation of the onset of turbulence by minor viscosity contrasts," Phys. Rev. Lett. **87**, 174501 (2001).

[27] K. C. Sahu, H. Ding, P. Valluri, and O. K. Matar, "Linear stability analysis and numerical simulation of miscible channel flows," Phys. Fluids **21**, 042104 (2009).

[28] B. Selvam, S. Merk, R. Govindarajan, and E. Meiburg, "Stability of miscible core-annular flows with viscosity stratification," J. Fluid Mech. **592**, 23 (2007).